A Study of the Trade-off Between Reducing Precision and Reducing Resolution for Data Analysis and Visualization

Duong Hoang, Pavol Klacansky, Harsh Bhatia, Peer-Timo Bremer, Peter Lindstrom, Valerio Pascucci

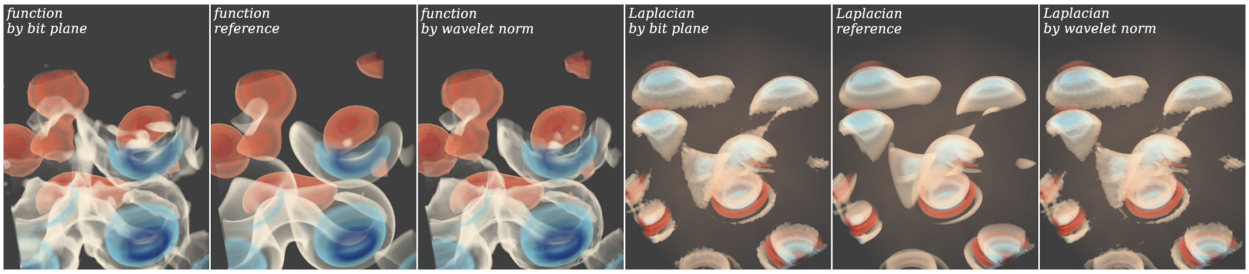

Fig. 1: Visualization of the *diffusivity* field at 0.2 bits per sample (bps) and its Laplacian field at 1.5 bps, using two of the bit streams studied in the paper. Compared to the *by bit plane* stream, the *by wavelet norm* stream produces a better reconstruction of the original function (left, compare white features), and a slightly worse, if not comparable, reconstruction of the Laplacian field (right).

Abstract—There currently exist two dominant strategies to reduce data sizes in analysis and visualization: reducing the *precision* of the data, e.g., through quantization, or reducing its *resolution*, e.g., by subsampling. Both have advantages and disadvantages and both face fundamental limits at which the reduced information ceases to be useful. The paper explores the additional gains that could be achieved by combining both strategies. In particular, we present a common framework that allows us to study the trade-off in reducing precision and/or resolution in a principled manner. We represent data reduction schemes as progressive *streams* of bits and study how various bit orderings such as by resolution, by precision, etc., impact the resulting approximation error across a variety of data sets as well as analysis tasks. Furthermore, we compute streams that are optimized for different tasks to serve as lower bounds on the achievable error. Scientific data management systems can use the results presented in this paper as guidance on how to store and stream data to make efficient use of the limited storage and bandwidth in practice.

Index Terms—data compression, bit ordering, multi-resolution, data analysis

1 Introduction

As the gap between the available compute power and the cost of data movement increases, data transfer, whether from cache, main memory, or disk, becomes a major bottleneck in many workflows. However, it has been shown that not every bit of data is always necessary to answer scientific questions with required accuracy. In particular, for techniques at the end of scientific workflows, such as visualization and data analysis, lower fidelity representations of the data often provide adequate approximations [24, 38, 70]; even during simulation, some loss in precision is often acceptable [9,38]. As a result, several different techniques have been proposed to reduce the size of data.

Broadly, these techniques either (i) reduce the data resolution, e.g., the number of data points stored, or (ii) reduce the precision of each data point. Examples of the first kind of approach are subsampling [49], adaptive mesh refinement [5], octrees and other tree structures [55], and wavelets [70], and those of the second are various forms of compression [34, 36, 41, 43, 48, 56, 62]. Traditionally, multiresolution structures have been used to accelerate dynamic queries, e.g., in rendering [37], since discarding data points based on the viewpoint or data complexity can result in significant speed-up. Compression based on quantization, on the other hand, is more common when storing data, where in the absence of other information, treating each sample as equally important is the null hypothesis. However, in many situations, a combination of both resolution and precision reduction may be appropriate. For example, high spatial resolution may be needed to resolve the topology of an isosurface, yet the corresponding data samples may be usable at less than full precision to adequately approximate the geometry. Conversely, accumulating accurate statistics may require high-precision values, yet a lower resolution subset of data points may be sufficient for the task.

In general, different levels of adaptivity in combinations of resolution and precision may be suitable for different types of analysis and visualization tasks, and for many, these requirements might be data dependent. Consequently, a globally optimal data organization may not exist. Instead, we consider a progressive setting in which some initial data is loaded and processed, and new data is requested selectively based on the requirements of the current task as well as the characteristics of the data already loaded. The result is a stream of bits ordered such that the error is minimized, considering the task at hand. However, although intuitively considering both resolution and precision in the ordering certainly has advantages, it is unclear how much the error could be reduced for a given data budget or how little data could be used to achieve the same error. Furthermore, optimal data-dependent orderings may be especially impractical since they assume perfect knowledge of the data. We therefore need to understand which of these potential gains are realizable. This paper aims to address these problems about the suitable bit orderings through extensive, empirical experiments. In particular, this paper presents:

- a framework that allows systematic studies of the resolution-versus-precision trade-off for common data analysis and visualization tasks. The core idea is to represent various data reduction techniques as bit streams that progressively improve data quality in either resolution or precision (Section 3). We can thus compare these techniques fairly, by comparing the

- *Hoang, Klacansky, and Pascucci are with the SCI Institute at the University of Utah, USA. E-mail: {duong, klacansky, pascucci}@sci.utah.edu*
- *Bhatia, Bremer, and Lindstrom are with Lawrence Livermore National Laboratory, USA. E-mail: {hbhatia, bremer5, pl}@llnl.gov*

Manuscript received 31 Mar. 2018; accepted 1 Aug. 2018.
Date of publication 16 Aug. 2018; date of current version 21 Oct. 2018.
For information on obtaining reprints of this article, please send e-mail to: reprints@ieee.org, and reference the Digital Object Identifier below.
Digital Object Identifier no. 10.1109/TVCG.2018.2864853

corresponding bit streams.

- empirical evidence that jointly optimizing resolution and precision can provide significant improvements on the results of analysis tasks over adjusting either independently. We present a diverse collection of data sets and data analysis tasks and also show how different types of data analysis might require substantially different data streams for optimal results.
- a greedy approach that gives estimations for lower bounds of error for various analysis tasks. In addition, we also identify practical streams that closely approximate these bounds for each task (Section 4.1, Section 4.2, Section 4.3, and Section 4.4) using a novel concept called *stream signature* (Section 3.4), which is a small matrix that captures the essence of how a bit stream navigates the precision-versus-resolution space.

In the third contribution, we focus on common analysis tasks, with a notable omission of volume rendering, which is dependent on many parameters, such as transfer function, camera position, and resolution of the image, among others. Thus, for volume rendering, a standalone study is likely required to ensure scientifically sound experiments with generalizable results.

2 Related work

Tree-based multiresolution hierarchies. A very common scheme to generate a tree-like hierarchy is to construct low-resolution copies of the data from higher resolution ones through downsampling. Examples include Gaussian and Laplacian pyramids [8] and mipmaps [37, 51]. The data is often stored in blocks on each resolution level. To save bandwidth, low-resolution versions of distant blocks can be streamed during rendering. However, these methods increase storage requirements, making them unsuitable for very large data. Recent multiresolution techniques save storage by adapting to the data in such a way that different regions are stored with different resolutions. A very popular approach is sparse voxel octrees [16, 25] and variations [6, 22, 31]. Smooth-varying regions are stored at coarser octree levels, which significantly reduces storage. During rendering, blocks of samples are streamed from an appropriate resolution, determined by how far the queried samples are from the eye/camera. A sparse, multiresolution hierarchy can also be built using other trees such as B+ tree [46] and kd-tree [21, 69], or space-filling curves [26, 49], which reorder data samples to form a hierarchy without any filtering steps or redundant samples. Low-resolution levels are constructed via subsampling, which, unfortunately, is prone to aliasing problems.

Transform-based multiresolution hierarchies. Other multiresolution approaches reduce data by transform-based compression. For example, COVRA [24] constructs an octree of bricks (consisting of blocks) and learns a sparse representation for the blocks in terms of basis blocks. Similarly, Fout et al. [23] transform each block using the KLT transform to produce several resolution levels, and compress each level using vector quantization [48]. Schneider et al. [56] also use vector quantization but with a simple Haar-like transform that separates each block of 2^3 voxels into one average and seven difference coefficients. Other examples of transform-based hierarchies include works that use the Tucker decomposition [2, 3, 59, 60], which decomposes the input data (stored as a tensor) into n matrices of basis vectors and one core tensor. Tensor decomposition works for higher dimensional data and can achieve high compression ratios, albeit at the price of a costly transform step.

Wavelets. Transforms that use fixed bases avoid such high computation cost at the expense of slightly less effective compression. Perhaps the most popular transform that uses a fixed basis is the (discrete) wavelet transform (DWT), which constructs a hierarchy of resolution levels via low and high bandpass filters. The transform is recursively applied to the lower resolution band, resulting in a hierarchy of "details" at varying resolution. The DWT is merely a change of basis that does not increase the data size. Furthermore, the wavelet basis functions are defined everywhere in space, requiring no special interpolation rules when given some arbitrary subset of wavelet coefficients. One disadvantage of the DWT is the random access cost, which is not constant time, although there has been work to develop acceleration structures to speed up local queries [67].

Besides offering a multiresolution decomposition, enabling data streaming with level-of-detail support, wavelet coefficients are especially amenable for compression, through thresholding or entropy compression. In storing and visualizing scientific data, wavelets (with compression) are used in a wide variety of systems [12, 13, 70] and applications, such as volume rendering with level-of-detail [29, 30, 33, 47, 68], turbulence visualization [65], and particle visualization [52].

Most wavelet-based techniques employ tiling of wavelet coefficients in individual subands to facilitate random access and spatial adaptivity in resolution. For example, the VAPOR toolkit [13] incorporates a multiresolution file format based on wavelets to allow data analysis on commodity hardware by storing individual tiles in separate files to allow loading of the region of interest. However, like most multiresolution work, only the resolution control is leveraged. The precision axis, which can potentially further reduce data transfer, is left unexplored.

Wavelet coders. Most work that explores the precision axis can be found in wavelet coders. Wavelet coefficients in corresponding regions across subbands can be thought of as belonging to a "tree". The embedded zerotrees (EZW) coder exploits the observation that in such trees, "parent" coefficients are often larger in magnitude than their "children". EZW therefore locates trees of wavelet coefficients that are insignificant with regard to a series of thresholds and encodes such a tree with one single symbol. The thresholds are typically set at the bit planes, starting from the most significant one. In this way, the data can be progressively refined in precision during decompression. The SPIHT coder [54] improves on EZW by locating more general types of zero trees [10]. SPECK [50] extends SPIHT to also exploit spatial correlations among nearby coefficients on the same subband.

Floating-point compression. The ZFP compression scheme [41] also encodes transform coefficients by bit plane, in order of decreasing significance. By partitioning the domain into $4 \times 4 \times 4$ independent blocks, ZFP supports fixed-rate compression, random access to the data, localized decompression, and fast inline compression. Extensions of ZFP allow it to vary either the bit rate or precision spatially over the domain, albeit at fixed resolution [42]. Other notable compression schemes for scientific data include scalar quantization encoding (SQE) [34], ISABELA [36], SZ [62], and FPZIP [43], which generally employ prediction and compress the residuals. ISABELA and SZ perform residual scalar quantization, whereas FPZIP truncates floats, which can be seen as nonuniform scalar quantization. Similarly, the precision-based level of details (PLoD) scheme proposed in MLOC [26] also truncates floats by dividing a double-precision number into several parts. MLOC includes a multiresolution scheme based on Hillbert curves, but this scheme (based on resolution) and the PLoD scheme (based on precision) are exclusive.

Mixing resolution and precision. Schemes that allow progressive data access in both resolution and precision include SBHP [11] and JPEG2000 [64]. Both partition each subband into blocks and code each block independently, in bit plane order. By interleaving compressed bits across blocks, one can construct a purely resolution-progressive or a purely precision-progressive stream, or anything in between. JPEG2000 has found use in the compression of scientific data, e.g., by Woodring et al. [70]. Since most JPEG2000 implementations are limited to integer data, the authors apply uniform scalar quantization to convert floating point data to integer form. Even though JPEG2000 supports varying both resolution and precision, most works do not explore this capability but focus only on setting bit rate. In general, efficiently leveraging both axes of data reduction has not been well studied.

Error quantification. Several works have aimed at quantifying the error incurred by data reduction, by compression or otherwise, for the results of analysis tasks. Baker et al. [1] evaluate several compressors, including FPZIP [43] and ISABELA [36] on ensembles of climate simulation data. Laney et al. [38] study the effects of lossy compression on the Miranda hydrodynamic simulation code. Li et al. [39] measure the error incurred by wavelet compression on turbulent-flow data. Wang et al. [66] assess the quality of distorted data using a combination of statistical metrics in the wavelet transform domain. Etiene et al. have published a series of studies on verification of isosurfaces in geometrical [20] and topological [19] terms, and verification of volume-rendered images [18]. They focus on order-of-accuracy and convergence analysis, where errors are introduced mostly through discretization, not necessarily for the purpose of reducing data bandwidth. For volume rendering, Ljung et al. [44] compute an error estimate based on color variation between low- and high-resolution levels in each block, which guides the selection of an appropriate resolution level for every block. Finally, the Z-checker framework [63] consists of a wide range of independent metrics to evaluate data quality after lossy compression. In all these works, errors are not quantified in the context of the tradeoff between resolution and precision.

Finally, for surveys of data reduction techniques in general, we refer the readers to the work of Rodríguez et al. [4] and Li et al. [40].

3 Data Reduction Schemes as Packet Streams

In order to systematically study the resolution-versus-precision trade-offs among different data reduction schemes, it is important to perform fair and consistent comparisons. In this section, we develop such a consistent methodology by proposing to model different data reduction schemes as *streams* of uniformly sized data *packets*, where the original data contains all the packets, and any reduction step removes a set of packets (comparable amounts of data). These data streams are transmitted using a client-server model. At any point, the client is assumed to have received a subset of packets (in some predetermined sequential order or in some order requested by the client), which can be used to reconstruct an approximation to the original data. Therefore, to compare different streams, we reconstruct the original data using the *same number* of packets from each stream and perform desired tasks on each of the (approximate) reconstructions. A stream is considered better suited for a given task if it produces results that are closer to the reference results computed from the original data. Fig. 2 gives a schematic view of our data streaming model.

Although both the server and the client in our model can be on the same physical machine, only the server has full knowledge of the data. Thus, when the client receives a packet, it might not know where that packet should be deposited. A common solution is to have both the client and the server agree beforehand on a static ordering of packets, independent of the data. We use the term *data-independent streams* to refer to streams using such solutions. In contrast, for *data-dependent streams*, an additional mechanism is needed to inform the client about the subbands and bit planes of incoming packets. In this paper, we consider both types of streams, as well as specialized *task-dependent* streams optimized for given tasks (see Table 1).

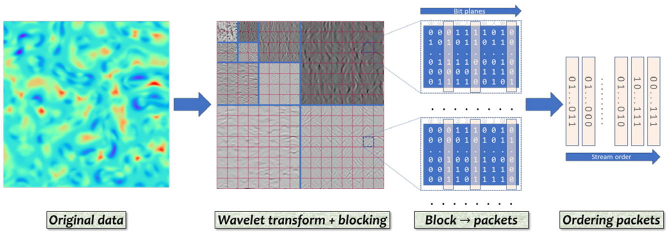

Fig. 2: Our data streaming model. The input is a regular grid of floating-point samples; the output is a stream of *packets*. A packet consists of bits from the same bit plane, from a block of negabinary wavelet coefficients. Different data reduction schemes generate different streams. The wavelet subbands are separated by blue lines in the second image, with the coarsest subband at the top left corner. Quantization and negabinary conversion happen immediately after wavelet transform.

Symbol	Name	Data Dependent	Task Dependent
$\mathcal{S}_{\text{lvl}}$	*by level*	✗	✗
$\mathcal{S}_{\text{bit}}$	*by bit plane*	✗	✗
$\mathcal{S}_{\text{wav}}$	*by wavelet norm*	✗	✗
$\mathcal{S}_{\text{mag}}$	*by magnitude*	✓	✗
$\mathcal{S}_{\text{[task]-opt}}$	*task-optimized*	✓	✓
$\mathcal{S}_{\text{[task]-sig}}$	*by signature*	✓/✗	✓/✗

Table 1: We define various types of data streams, including data-independent, data-dependent, task-independent, and task-dependent streams. $\mathcal{S}_{\text{[task]-sig}}$ can be data dependent or task dependent, depending on the stream from which it is derived.

3.1 Decomposition of Data into Packets

Although one way to compare different data reduction strategies is to restrict the techniques to the same data size and compare data quality, it is difficult to enforce consistency. For example, the amount of change (in data) in one step of multiresolution simplification may be different from removing one bit in the quantization of every sample. To make all data reduction schemes comparable, in each scheme, a data set is redefined as a stream of equally sized *packets*. These packets are the smallest units of data transfer in our framework. A packet consists of a relatively small number $(\approx 2^3)$ of bits and is associated with a resolution level and a precision level (i.e., bit plane). In this framework, different data-reduction schemes become different orderings of packets, called *streams*. Restricting two (or more) data streams to the same number of packets allows us to perform fair and consistent comparisons.

Resolution levels. Although there exist several ways to define the notion of resolution/scale/frequency, we choose the multilevel basis functions of the wavelet transform because they have compact support, and they avoid interpolation problems associated with other representations. Wavelet transform enables spatial adaptivity (i.e., finer resolution in regions that contain sharp features, at the expense of coarser resolution elsewhere). In particular, we choose the CDF5/3 multilinear wavelets [14] for their balance between simplicity and effectiveness at decorrelating the input signal in practice [64].

A multidimensional wavelet transform can be performed in multiple passes, which partitions the original domain into *subbands*, each of which can be thought of as a resolution level associated with one or more spatial direction. One transform pass (in 3D) creates eight subbands, of which the first is a low-pass, downsampled version of the original data, and the remaining add fine details in each subset of the dimensions (see Fig. 2 for a visualization of subbands in 2D). A subsequent transform pass recurses only on the first subband (of the previous level), creating the next (resolution) level of subbands. We use l $(0 \leq l < L)$ to index the subbands, with $l = 0$ referring to the coarsest subband and L denoting the number of subbands. In 3D, the eight subbands created after one transform pass are indexed in the following order, from coarse to fine: LLL, LLH, LHL, LHH, HLL, HLH, HHL, HHH (L stands for “low” and H stands for “high”, referring to the low- and high-pass filter pair that perform the wavelet transform). The LHL subband, for example, contains coefficients that are low-pass transformed along X and Z, and high-pass transformed along Y. In our experiments, the number of subbands, L, is fixed at $1+3*7=22$, corresponding to three transform passes in 3D.

Precision levels. For creating packets corresponding to different precision levels, we quantize floating-point wavelet coefficients to B-bit signed integers. For most of the experiments in this paper, $B = 16$. This quantization eliminates the floating-point exponent bits, such that every bit (except the sign bit) can be associated with a bit plane b $(0 \leq b < B)$. In our convention, the higher indexed bit planes are less significant. We convert quantized coefficients to the negabinary representation, where integers are represented in base -2, i.e., $\sum_{b=0}^{B} c_b(-2)^b$ with $c_b \in \{0,1\}$. Negabinary encoding is preferred over two’s complement encoding, because we start data reconstruction by zero-initializing all bits, and negabinary encoding has no single dedicated sign bit and ensures that small coefficients have many leading zero-bits. This transformation increases the number of bit planes by one, i.e., $0 \leq b \leq B$.

Blocks and packets. Precisely, a *packet* consists of bits from the same bit plane, from a *block* of negabinary wavelet coefficients. A block is a $[g \times g \times g]$ grid of adjacent coefficients from the same subband. We let g be a constant ($g = 2$ in this paper), so that finer resolution subbands contain more packets, which presents a trade-off between packets that provide wider (but coarser) coverage and packets that provide finer (but more local) details. Every packet (of size one byte in this paper) comes from a bit plane b and a subband l. g is chosen to be larger than one for performance reasons, as in practice, most systems read bits in batches.

3.2 Data-Dependent and Data-Independent Streams

We define two streams: *by level* and *by bit plane*, which model two common reduction schemes in the literature. The *by level* stream, $\mathcal{S}_{\text{lvl}}$, orders the packets strictly from coarser to finer subbands. Within the same subband, packets follow the row-major order of blocks and then bit plane order (from 0 to B) within each coefficient. All bits for each coefficient are streamed together. The other common ordering, *by bit plane*, or $\mathcal{S}_{\text{bit}}$, proceeds strictly from higher ordered to lower ordered bit planes. Within the same bit plane, packets follow the subband order (from 0 to $L-1$) and then row-major order in each subband. $\mathcal{S}_{\text{lvl}}$ and $\mathcal{S}_{\text{bit}}$ are designed to mimic the way data is accessed in traditional methods that work either in resolution ($\mathcal{S}_{\text{lvl}}$) or in precision ($\mathcal{S}_{\text{bit}}$).

Additionally, we define a third stream that combines these two dimensions and refer to it as *by wavelet norm*, or $\mathcal{S}_{\text{wav}}$. This stream orders packets in descending order of weights $w_{\text{wav}}(p) = 2^{B-b(p)} \times \|\psi_{l(p)}\|$, where p denotes a packet and $\psi_{l(p)}$ represents wavelet basis on subband $l(p)$. The $\|\|$ notation refers to the L_2 norm of the wavelet basis function. The first term captures the contribution of a bit on bit plane $b(p)$, and the second term captures the contribution of a wavelet coefficient on subband $l(p)$. In the wavelet representation, a function f is written as a linear sum of wavelet basis functions, i.e., $f = \sum c_i \psi_i$, where c_i are the coefficients. Since our wavelet transforms are based on lifting, this norm is usually not one, but it increases with level. Basis functions in the same subband share the same norm, hence $w_{\text{wav}}(p)$ is simply the contribution (in L_2 norm) of a bit on bit plane $b(p)$ and subband $l(p)$, to the whole function f. This ordering based on norms of wavelet basis functions was proposed previously by Weiss et al. [67]. For details of computing the norms of basis functions, see Appendix A.

Another common way to reduce data in the wavelet domain is to leave out the coefficients of the smallest magnitudes. Note that coefficient magnitudes are only weakly related to error, as the error also depends on the wavelet basis function norm [67]. We model this scheme with a stream called *by magnitude*, or $\mathcal{S}_{\text{mag}}$. Here, the weight function is $w_{\text{mag}}(p) = \sum_{c \in \text{block}(p)} \|c\|$ (the sum is over all coefficients in the block that contains packet p). If two packets have the same weight, they are ordered by subband index and then by bit plane.

Unlike $\mathcal{S}_{\text{lvl}}$, $\mathcal{S}_{\text{bit}}$, and $\mathcal{S}_{\text{wav}}$, the $\mathcal{S}_{\text{mag}}$ stream is data dependent because the coefficient magnitudes are not known without the data. In principle, data-dependent streams are better than data-independent streams because they can prioritize important packets based on the actual data. However, data-dependent streams are ill-suited for practical purposes, because the cost of sending position information likely outweighs any potential benefit. Nevertheless, we study them for various reasons. First, the *by magnitude* scheme is well known in the literature [13]. Second, the "best" data-dependent streams (which do not include position information for packets) can serve as a baseline to evaluate the performance of their data-independent counterparts. Finally, in addition to being data dependent, streams can also be task dependent (Section 3.3), which may provide insights into how data should be queried to perform certain analysis tasks.

3.3 Task-Optimized Streams

Each analysis task may require a fundamentally different stream for optimal results. Studying such "optimal" streams is important because they not only serve as a baseline but also can provide insights into other, more practical streams. Given the original data set f and its reconstructed approximation f' using a subset of packets, let q represent some quantity of interest, e.g., histogram, isosurface, etc., computed on f or f'. For a given q, a well-defined error metric $e(q(f'), q(f))$, which returns a single scalar, is needed. Given f, q, and e, our goal is to generate an *optimal* (and data-dependent) stream, $\mathcal{S}_{\text{opt}}$, for q with respect to e. One possible definition for $\mathcal{S}_{\text{opt}}$ is a stream such that the area under the plotted curve of e, with respect to the number of bits, is minimized for all packets to be streamed. However, this definition is limited in practice because a stream should be able to terminate at any point and still produce as small an error as possible.

Instead, we employ a greedy approach to define the optimal stream. We notice through experiments, however, that a straightforward greedy algorithm can pick unimportant packets too early. For example, starting with an all-zero reconstruction $f' = 0$ and an empty stream, we can repeatedly append new packets to the stream, which when included in the current f', would minimize e at every step. At some point, the algorithm might pick a packet that introduces the lowest error yet contributes very little to improve the quality of f' (because more important packets would increase the error), leading to a nonoptimal stream. To avoid this problem, we make a modification to this greedy algorithm and build the stream backwards. We start with a "lossless" f' (i.e., $f' = f$), and at each step we remove the packet that has the least impact on the error e from f'. This modification largely avoids the previous problem where less important packets were added to $\mathcal{S}_{\text{opt}}$ too early, because by starting with the full (instead of empty) set of packets, our error measurement better captures the importance of packets.

Unfortunately, such a greedy algorithm is still expensive in practice, as its complexity is at least $\mathcal{O}(n^2)$ (n is the number of packets), due to the 2-level nested loop. For a $nx \times ny \times nz$ volume, a block size of $bx \times by \times bz$, and $B+1$ bit planes, n is $\frac{nx}{bx} \times \frac{ny}{by} \times \frac{nz}{bz} \times (B+1)$. Thus, even a small volume, e.g., $nx, ny, nz = 64$ and $bx, by, bz = 2$, can result in a prohibitively high run time, as $n^2 = (32768 \times 17)^2$. Therefore, we adopt a simplified version of this algorithm, where only one pass through n packets is needed. In iteration i ($0 \le i < n$), we set a new packet p_i to zero, compute and record the incurred error w_i using the error metric e, and then enable p_i again at the end of iteration i. After n iterations, each packet has an associated weight w_i. The stream $\mathcal{S}_{\text{opt}}$ is simply the sorted list of packets in decreasing order of the weights. This simplified algorithm (Algorithm 1) has significantly lower running time, while (by observation) retaining the same quality for $\mathcal{S}_{\text{opt}}$.

Algorithm 1 Computing a task-optimized stream

```
 1: Inputs:
        An original function $f$
        An unordered set of $n$ packets $P = \{p_i\}$, produced from $f$
        A quantity of interest $q$, and an error function $e$
 2: Initialize:
        A set of $n$ weights $\{w_i\}$
 3: for each packet $p_i$ do
 4:     $p_i := 0$
 5:     $P \to$ wavelet coefficients $C = \{c_j\}$
 6:         (inverse quantization and inverse negabinary transform)
 7:     $\{c_j\} \to f'$ (inverse wavelet transform)
 8:     $w_i := e(q(f'), q(f))$
 9:     Restore $p_i$
10: end for
11: Sort the $p_i$'s in descending order of $w_i$.
12: Output:
        The $q$-optimized stream, which is the sorted $P$
```

For a more optimized implementation, the inverse wavelet transform on line 7 can be replaced by "splatting" coefficient p_i onto the domain, due to the transform being linear and the fact that p_i is the only coefficient changed in the current iteration. Since tt is almost never advantageous to stream bits belonging to one coefficient out-of-order, we also enforce that in the final stream, packets belonging to the same group follow the bit plane order (from 0 to B).

3.4 Stream Signatures

Unlike data-independent streams, data-dependent streams do not impose a static ordering of packets. To concisely represent and characterize the dynamic ordering of data-dependent

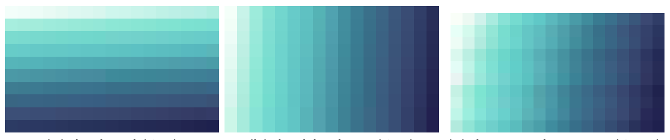

Fig. 3: Visualization of signatures for $\mathcal{S}_{\text{lvl}}$, $\mathcal{S}_{\text{bit}}$, and $\mathcal{S}_{\text{wav}}$ in 2D. Each signature is a 10×17 image, corresponding to 10 subbands (in 2D) and 17 bit planes. Each (l,b) "cell" contains a unique value from 0 to 169, indicating its "priority" in the stream, and is mapped to a white–blue color scale. $\mathcal{S}_{\text{lvl}}$ streams bits by resolution (from top to bottom), $\mathcal{S}_{\text{bit}}$ streams by precision (from left to right), while $\mathcal{S}_{\text{wav}}$ mixes precision and resolution.

streams, we introduce the notion of a *stream signature*. Any stream can be represented with respect to the two-dimensional space of resolution (subbands) and precision (bit planes), i.e., $\mathbb{L}_{L,B} = \{(l,b) \mid 0 \le l < L,\ 0 \le b \le B\}$. Given a stream, we define its signature A as an $L \times (1+B)$ matrix, where each (l,b) element is associated with $P_{l,b}$, the set of packets belonging to subband l and bit plane b. In particular, $A(l,b)$, i.e., the (l,b) element of A, is an integer in the range $[0,(1+B)\times L)$, and indicates, on average, the position at which packets in $P_{l,b}$ appear in the given stream. For example, the signature $A = \left[\begin{smallmatrix}0&1&4\\2&3&5\end{smallmatrix}\right]$ indicates that the stream begins with packets that lie on the first bit plane of the first subband, as $A(0,0) = 0$. Those are followed by packets on the second bit plane of the first subband ($A(0,1) = 1$), and then the first bit plane of the second subband ($A(1,0) = 2$), and finally, the third bit plane of the second subband ($A(1,2) = 5$). Thus, a stream's signature shows how the stream traverses the space $\mathbb{L}_{L,B}$ and highlights the different resolution-versus-precision trade-offs among streams, especially among $\mathcal{S}_{\text{opt}}$ streams optimized for different tasks. In Fig. 3 we visualize the signatures of $\mathcal{S}_{\text{bit}}$, $\mathcal{S}_{\text{lvl}}$, and $\mathcal{S}_{\text{wav}}$, defined in Section 3.1.

To compute a stream signature, we partition the whole domain (not individual subbands) into several *regions*, compute one signature per region, and average these local signatures. Partitioning is used since it is only when packets are relatively well localized that their relative ordering in the $\mathbb{L}_{L,B}$ space becomes meaningful. For example, a packet at one corner of the domain may be streamed before one at an opposite corner, but this fact contains no useful information. We define a region to be the spatial volume that is covered by a packet in the coarsest subband. Algorithm 2 lists the steps of our approach.

Finally, a signature can be used to construct a stream denoted generically as $\mathcal{S}_{\text{sig}}$. This construction is done by iterating through each element $A(l,b)$ in ascending order and adding to the end of $\mathcal{S}_{\text{sig}}$ all the packets in $P_{l,b}$. An $\mathcal{S}_{\text{sig}}$ captures the behavior (in the $\mathbb{L}_{L,B}$ space) of the stream it derives from, but it is stripped from any spatial adaptivity. Hence, when $\mathcal{S}_{\text{sig}}$ is derived from an $\mathcal{S}_{\text{opt}}$, it can serve as a bridge when comparing the resolution-versus-precision trade-offs between data-independent and data-dependent streams.

Algorithm 2 Computing a stream signature

```
 1: Inputs:
        A stream $P = \{p_i\}$
 2: Initialize:
        Per-region signature matrix $A_r := 0$
        Global signature matrix $A := 0$
 3: for each packet $p_i$ in $P$ do
 4:     Let $r$, $b$, $l$ be the region, bit plane, and subband that $p_i$ belongs
 5:     $A_r(l,b) := A_r(l,b) + i$
 6: end for
 7: for each region $r$ do
 8:     Sort the elements of $A_r$
 9:     Assign each element of $A_r$ its index after sorting
10:     $A := A + A_r$
11: end for
12: Sort the elements of $A$
13: Assign each element of $A$ its index after sorting
14: Output:
        The signature matrix $A$
```

Name	Type	Data type
boiler [58]	combustion simulation	float64
plasma [28]	magnetic reconnection simulation	float32
diffusivity [15]	hydrodynamics simulation	float64
pressure [15]	hydrodynamics simulation	float64
turbulence [17]	fluid dynamics simulation	float32
kingsnake [27]	CT scan	uint8
foam [45]	CT scan	uint16

Table 2: Data sets used in our experiments; all volumes are 64^3. Additional data sets are included in the supplementary material.

4 Evaluation on Different Analysis Tasks

Thus far, we have presented several types of streams: data-independent ($\mathcal{S}_{\text{lvl}}$, $\mathcal{S}_{\text{bit}}$, $\mathcal{S}_{\text{wav}}$), data-dependent and task-independent ($\mathcal{S}_{\text{mag}}$), and task-dependent ($\mathcal{S}_{\text{opt}}$, $\mathcal{S}_{\text{sig}}$). In this section, we consider a variety of common analysis and visualization tasks to evaluate the performance of these streams. For each task, we define an error metric, e, for the evaluation and comparison of streams. Using Algorithm 1, we compute streams specifically optimized for each task, $\mathcal{S}_{\text{[task]-opt}}$, and use its signature to compute the corresponding $\mathcal{S}_{\text{[task]-sig}}$. For a variety of data sets, we compare these streams by evaluating the error as a function of bits per samples (or *bps*), defined as the total number of bits received divided by the total number of samples. To mimic the effects of entropy compression commonly used in practice, we remove from each stream all packets that consist only of leading-zero bits. The wavelet basis allows us to always reconstruct data at full resolution, which greatly simplifies computation of errors, as there exists no standard method to compute error between grids of different dimensions.

4.1 Function Reconstruction

One of the most fundamental analysis tasks is that of reconstructing the original function itself. A commonly used error metric in this case is the root-mean-square error (RMSE). Fig. 4 shows a comparison of the different streams for a variety of data sets. It can be noted that, in general, $\mathcal{S}_{\text{rmse-opt}}$ (the stream optimized to minimize the RMSE) performs better than $\mathcal{S}_{\text{rmse-sig}}$ due to spatial adaptivity, whereas $\mathcal{S}_{\text{rmse-sig}}$ slightly outperforms $\mathcal{S}_{\text{wav}}$, followed by $\mathcal{S}_{\text{bit}}$, $\mathcal{S}_{\text{mag}}$, and $\mathcal{S}_{\text{lvl}}$. In particular, $\mathcal{S}_{\text{bit}}$ outperforms $\mathcal{S}_{\text{lvl}}$ (for *kingsnake* and *boiler*, it does so after approximately 1 bps), which can be attributed to the removal of leading-zero packets. Empirically, wavelet coefficients on finer scale subbands are much smaller in magnitude [54]. Such coefficients contain a majority of the leading-zero bits, whose removal benefits $\mathcal{S}_{\text{bit}}$ the most. *diffusivity* and *plasma* contain a significant amount of empty space, which translates to more leading-zero bits after the wavelet transform that $\mathcal{S}_{\text{bit}}$ can take advantage of, and thus, it outperforms $\mathcal{S}_{\text{lvl}}$ immediately from the beginning.

$\mathcal{S}_{\text{mag}}$ underperforms for the same reason that $\mathcal{S}_{\text{lvl}}$ does, but to a lesser extent, since $\mathcal{S}_{\text{mag}}$ is adapted to the data. $\mathcal{S}_{\text{wav}}$ outperforms both $\mathcal{S}_{\text{lvl}}$ and $\mathcal{S}_{\text{bit}}$, because it follows the optimal (data-independent) bit ordering in $\mathbb{L}_{L,B}$ in the L_2 norm, which is also the norm that the RMSE is based upon. Unsurprisingly, $\mathcal{S}_{\text{rmse-opt}}$ outperforms all the others, as it is the most data-adaptive (i.e., it can optimize packet ordering in the spatial domain in addition to the $\mathbb{L}_{L,B}$ domain). $\mathcal{S}_{\text{rmse-sig}}$ is the second best stream, as it follows the bit ordering of $\mathcal{S}_{\text{rmse-opt}}$ in $\mathbb{L}_{L,B}$ but lacks any spatial adaptivity. In general, $\mathcal{S}_{\text{wav}}$ and $\mathcal{S}_{\text{sig}}$ have similar performances, but $\mathcal{S}_{\text{sig}}$ performs better when the data is less smooth or noisy, as is the case for *boiler* and *kingsnake*. For such data, fine-level packets tend to have very few leading one bits among a majority of leading zero bits, which $\mathcal{S}_{\text{wav}}$ does not take into account (data-independent streams in effect assume every packet contains all one bits).

We explore the errors visually by rendering the *plasma* volume at 0.2 bps, for all streams except $\mathcal{S}_{\text{rmse-opt}}$ (Fig. 5). Although $\mathcal{S}_{\text{lvl}}$ has the precision to obtain an accurate background, it lacks resolution to resolve the fine details. $\mathcal{S}_{\text{bit}}$, instead, lacks the precision to reconstruct the (mostly smooth) background, but it has enough resolution to capture the fine details well. $\mathcal{S}_{\text{wav}}$ balances both precision and resolution, producing a more accurate picture as a whole. In this case, the $\mathcal{S}_{\text{sig}}$ stream produces the most accurate rendering overall.

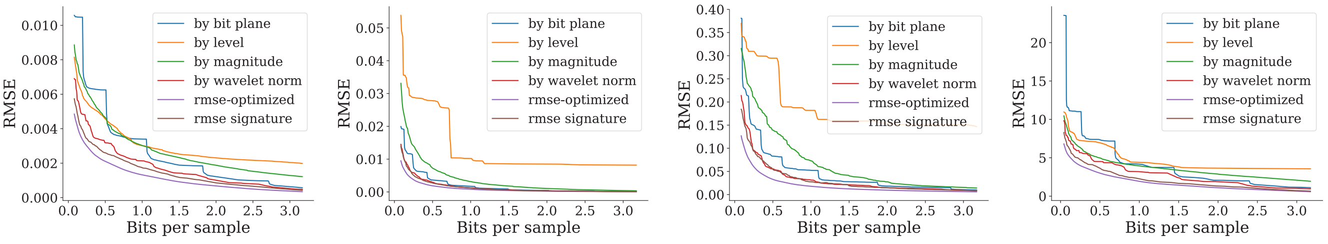

(a) *boiler* $[2.351e{-}9, 0.138]$ (b) *diffusivity* $[-0.848, 0.711]$ (c) *plasma* $[0.024, 14.67]$ (d) *kingsnake* $[63, 185]$

Fig. 4: Root-mean-square error (RMSE) of reconstructed functions for different streams and data sets; lower RMSE is better. The streams are truncated at both ends to highlight the differences, without omitting important information. The numbers in brackets are the ranges of original data samples. The general ordering of error, from lowest to highest, is $\mathcal{S}_{\text{opt}} < \mathcal{S}_{\text{sig}} < \mathcal{S}_{\text{wav}} < \mathcal{S}_{\text{bit}} < \mathcal{S}_{\text{mag}} < \mathcal{S}_{\text{lvl}}$.

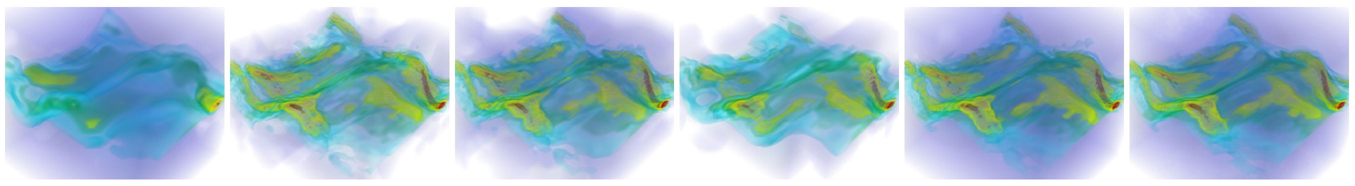

(a) *by level* ($\mathcal{S}_{\text{lvl}}$) (b) *by bit plane* ($\mathcal{S}_{\text{bit}}$) (c) *by wavelet norm* ($\mathcal{S}_{\text{wav}}$) (d) *by magnitude* ($\mathcal{S}_{\text{mag}}$) (e) *by signature* ($\mathcal{S}_{\text{sig}}$) (f) *reference*

Fig. 5: Volume renderings of a 64^3 region of *plasma* data set at 0.2 bps. $\mathcal{S}_{\text{lvl}}$ captures the background (purple-blue) well, whereas $\mathcal{S}_{\text{bit}}$ captures the fine details better. $\mathcal{S}_{\text{wav}}$ combines the strength of both. $\mathcal{S}_{\text{sig}}$, however, produces the most accurate rendering in overall.

4.2 Derivative Computation

Computation of derivative-based quantities is important in data analysis. Examples include vorticity (curl) computation from velocity fields to identify vortical structures, gradient computation for accurate Morse segmentation and shading, and ridge extraction (e.g., for Lagrangian coherent structures). In this paper, derivatives are always computed using finite differences, which is common in practice. In this section, we use 32 bits for quantization to ensure enough precision for finite differences. We always compute finite differences on the finest resolution grid to avoid computing distances between quantities defined on grids of different resolutions.

4.2.1 Gradient Computation

Given a function f defined on a grid, its gradient at a grid point $\mathbf{x} = (x,y,z)$ is $\nabla f(\mathbf{x}) = \left(\frac{\partial f}{\partial x}, \frac{\partial f}{\partial y}, \frac{\partial f}{\partial z}\right)$. For accuracy, we use a five-point stencil to compute the gradient, i.e., $\frac{\partial f}{\partial x} \approx \frac{1}{12} f(x-2,y,z) - \frac{2}{3} f(x-1,y,z) + \frac{2}{3} f(x+1,y,z) - \frac{1}{12} f(x+2,y,z)$, but we note that the relative performances of the streams stay the same, using the more common two- and three-point formulas. The error between a gradient field ∇f, and its low-bit-rate approximation $\nabla f'$, is defined as $e(\nabla f', \nabla f) = \sqrt{\frac{1}{N}\sum_{i=1}^{N} \|\nabla f'(\mathbf{x}_i) - \nabla f(\mathbf{x}_i)\|^2}$. Using Algorithm 1, we compute a *gradient-optimized* stream, $\mathcal{S}_{\text{grad-opt}}$, that minimizes the difference between the reconstructed and the original gradient fields.

Fig. 7 shows the gradient error incurred by different streams for four data sets. In general, we observe the ordering of performance (from best to worst) as: $\mathcal{S}_{\text{grad-opt}}$, $\mathcal{S}_{\text{grad-sig}}$, $\mathcal{S}_{\text{bit}}$, $\mathcal{S}_{\text{wav}}$, $\mathcal{S}_{\text{mag}}$, $\mathcal{S}_{\text{lvl}}$. This ordering can also be seen in Fig. 8, where the x-component of the gradient field for *tuburlence* is rendered at 0.3 bps. Unlike in the RMSE case, $\mathcal{S}_{\text{bit}}$ performs nearly the same as $\mathcal{S}_{\text{wav}}$. To investigate this difference, we extract a 1D line from the *plasma* data set and reconstruct the function using $\mathcal{S}_{\text{bit}}$ and $\mathcal{S}_{\text{wav}}$ at 0.6 bps (Fig. 6). $\mathcal{S}_{\text{wav}}$'s reconstruction is more accurate on average compared to $\mathcal{S}_{\text{bit}}$, which captures well the function's shape (due to the presence of fine-scale bits), but not the function values (due to the lack of precision in the coarse-scale coefficients). Functions reconstructed with $\mathcal{S}_{\text{bit}}$ tend to be "shifted" in the range domain, as seen in Fig. 6. However, the gradient operator has the tendency to cancel the shifting effect, bringing the performance of $\mathcal{S}_{\text{bit}}$ closer to that of $\mathcal{S}_{\text{wav}}$.

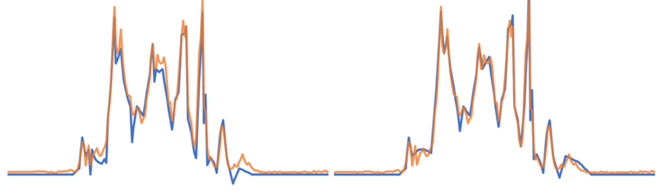

(a) *by bit plane* ($\mathcal{S}_{\text{bit}}$) (b) *by wavelet norm* ($\mathcal{S}_{\text{wav}}$)

Fig. 6: A 1D line extracted from *plasma*, and reconstructed using $\mathcal{S}_{\text{bit}}$ and $\mathcal{S}_{\text{wav}}$ at 0.6 bps. The original data is in orange and the reconstructions are in blue. $\mathcal{S}_{\text{bit}}$ is worse at capturing the function values (seen as a slight vertical shift) but it is comparable to $\mathcal{S}_{\text{wav}}$ in capturing the shape of the function, which is important for gradient computation.

$\mathcal{S}_{\text{grad-opt}}$ again outperforms the rest of the streams. $\mathcal{S}_{\text{lvl}}$ and $\mathcal{S}_{\text{mag}}$ perform poorly for gradient computation, lacking the resolution to capture sharp features. $\mathcal{S}_{\text{grad-sig}}$ mostly closely follows $\mathcal{S}_{\text{bit}}$ in performance but outperforms it for *boiler*. Again, compared to the other fields, *boiler* is less smooth, resulting in less spatial coherency in the magnitudes of the fine-scale coefficients, which $\mathcal{S}_{\text{grad-opt}}$ and $\mathcal{S}_{\text{grad-sig}}$ can take advantage of, whereas $\mathcal{S}_{\text{wav}}$ or $\mathcal{S}_{\text{bit}}$ do not take into account actual bit values. Overall, the results suggest that besides minimizing RMSE, $\mathcal{S}_{\text{wav}}$ also works well for gradient computation, although for the latter task, $\mathcal{S}_{\text{bit}}$ is also good alternative.

4.2.2 Laplacian Computation

The Laplace operator is a second-order differential operator defined as the divergence of the gradient field. The Laplacian of a 3D field is defined as $\Delta f = \frac{\partial^2}{\partial x^2} f + \frac{\partial^2}{\partial y^2} f + \frac{\partial^2}{\partial z^2} f$. Using a five-point finite difference, we approximate $\frac{\partial^2 f}{\partial x^2} \approx -\frac{1}{12} f(x-2,y,z) + \frac{4}{3} f(x-1,y,z) - \frac{5}{2} f(x,y,z) + \frac{4}{3} f(x+1,y,z) - \frac{1}{12} f(x+2,y,z)$. We use the root-mean-square error to compare two Laplacian fields, i.e., $e(\Delta f', \Delta f) = \text{RMSE}(\Delta f', \Delta f)$. We use Algorithm 1 to compute a *Laplacian-optimized* stream, $\mathcal{S}_{\text{lap-opt}}$, which minimizes e, and an $\mathcal{S}_{\text{lap-sig}}$ stream from its signature. Fig. 9 plots the errors for all relevant streams. The plots here largely follow the ones in Fig. 7, in terms of relative performance among the streams, but with more discernible gaps between $\mathcal{S}_{\text{bit}}$ and $\mathcal{S}_{\text{lap-sig}}$, as well as between $\mathcal{S}_{\text{lap-sig}}$ and $\mathcal{S}_{\text{bit}}$. The results suggest that similar to the gradient case, computation of the Laplacian favors resolution over precision, but to a higher degree.

4.3 Histogram Computation

A histogram succinctly summarizes the distribution of sample values, and thus it is useful as a cursory "look" into the data and in guiding further analysis. For example, it can be used to guide the selection of colors and opacities in a transfer function. To decide on an error

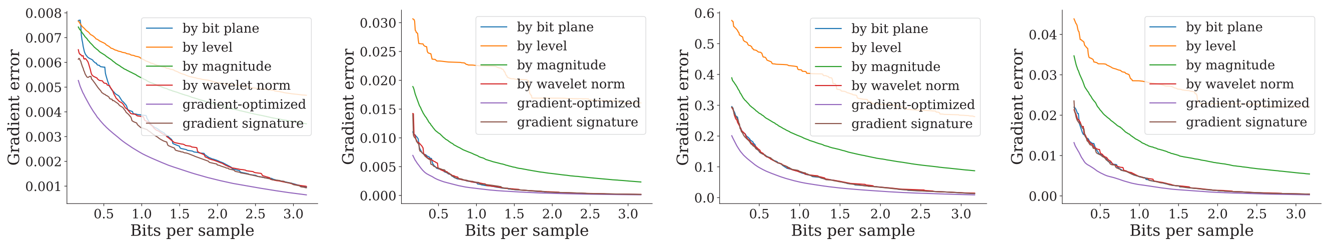

(a) *boiler*, $[2.020e{-}9, 0.148]$ (b) *diffusivity* $[1.063e{-}10, 0.497]$ (c) *turbulence* $[0.465e{-}3, 12.19]$ (d) *pressure* $[2.542e{-}6, 0.536]$

Fig. 7: Gradient error of reconstructed functions. Lower gradient error is better. Leading zero packets are removed, and the plots are truncated in the same way as in Fig. 4. The numbers in brackets are the ranges of original gradient magnitudes. The trend in error, in all cases, is $\mathcal{S}_{\text{grad-opt}} < \mathcal{S}_{\text{grad-sig}} \approx \mathcal{S}_{\text{bit}} \approx \mathcal{S}_{\text{wav}} < \mathcal{S}_{\text{mag}} < \mathcal{S}_{\text{lvl}}$.

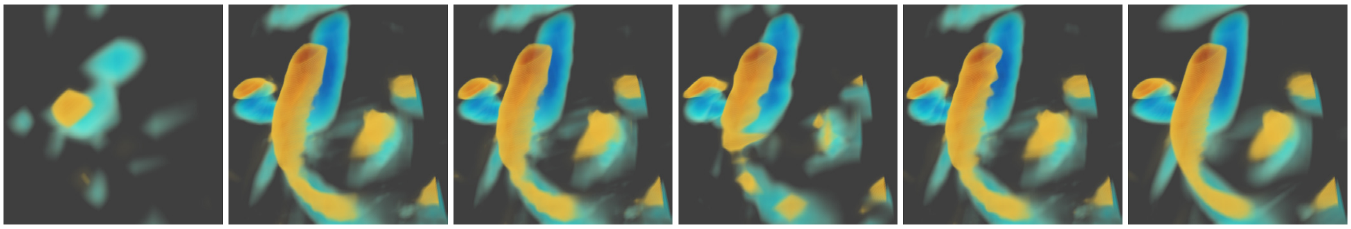

(a) *by level* ($\mathcal{S}_{\text{lvl}}$) (b) *by bit plane* ($\mathcal{S}_{\text{bit}}$) (c) *by wavelet norm* ($\mathcal{S}_{\text{wav}}$) (d) *by magnitude* ($\mathcal{S}_{\text{mag}}$) (e) *by signature* ($\mathcal{S}_{\text{grad-sig}}$) (f) *reference*

Fig. 8: The x-component of the (64^3) gradient field of *turbulence*, reconstructed at 0.3 bps. $\mathcal{S}_{\text{bit}}$, $\mathcal{S}_{\text{wav}}$, and $\mathcal{S}_{\text{grad-sig}}$ produce visually comparable gradient fields.

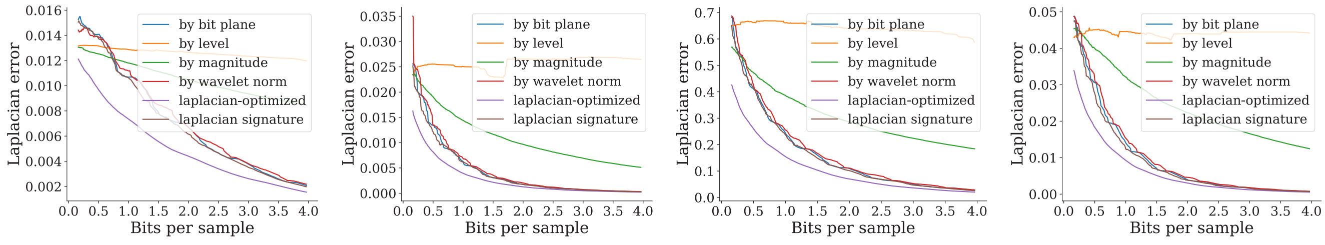

(a) *boiler* $[-0.393, 0.221]$ (b) *diffusivity* $[-0.404, 0.269]$ (c) *turbulence* $[-17.44, 11.99]$ (d) *pressure* $[-0.467, 0.432]$

Fig. 9: Laplacian error comparison among streams. The plots are truncated to better highlight differences without discarding important information. The numbers in brackets are the ranges of the original Laplacian fields. In all cases, in terms of error, $\mathcal{S}_{\text{lap-opt}} < \mathcal{S}_{\text{lap-sig}} < \mathcal{S}_{\text{bit}} < \mathcal{S}_{\text{wav}} < \mathcal{S}_{\text{mag}} < \mathcal{S}_{\text{lvl}}$.

metric to compare histograms, we experimented with several popular metrics such as Kolmogorov-Smirnov [57], Kullback-Leibler [35], and Earth Mover's Distance [53], among others [7,32]. We chose histogram intersection [61] as the metric of choice, because it is fast to compute and is reasonably insensitive to changes in precision, as well as the number of bins. The intersection distance between two histograms H_1 and H_2 is defined as $e(H_1, H_2) = 1 - \sum_i \min(H_1(i), H_2(i))$ (the sum is over all bins i). Every histogram is normalized by dividing the value in each bin by the total number of samples. We decided that the error metric should take into account both the histogram shapes and the range of values, and we clamped the range of values in reconstructed functions to that of the original function, so that corresponding histogram bins, i.e., $H_1(i)$ and $H_2(i)$, share the same range.

As before, for each data set, we use Algorithm 1 to compute an $\mathcal{S}_{\text{hist-opt}}$ stream, optimized for histogram error, and then construct an $\mathcal{S}_{\text{hist-sig}}$ from its signature. We plot the error curves for all relevant streams using the Intersection error metric (compare Fig. 10). We use 64 for the number of bins but note that there exist no meaningful differences across a wide range of number of bins (from 64 to 512) in our experiments. In all cases, the group consisting of $\mathcal{S}_{\text{bit}}$, $\mathcal{S}_{\text{lvl}}$, and $\mathcal{S}_{\text{mag}}$ underperforms the other group by a large margin. $\mathcal{S}_{\text{mag}}$ performs poorly, because it ignores regions of smooth variations, which nevertheless count toward the distribution. $\mathcal{S}_{\text{lvl}}$ generally outperforms $\mathcal{S}_{\text{bit}}$ at low bit rates, although there are several crossover points between the two curves. As can be seen in Fig. 12, $\mathcal{S}_{\text{lvl}}$ outperforms $\mathcal{S}_{\text{bit}}$ when leading zero packets are present, because increasing resolution does not help as much as increasing precision. This is because the histogram is oblivious to spatial locations of samples (which require resolution to resolve) but is sensitive to sample values (which require precision). However, when leading zero packets are removed, $\mathcal{S}_{\text{bit}}$ benefits significantly more than $\mathcal{S}_{\text{lvl}}$ does (for the same reason explained in Section 4.1), resulting in the observed crossovers.

In the latter group, the performances of $\mathcal{S}_{\text{wav}}$ and $\mathcal{S}_{\text{hist-sig}}$ (and even $\mathcal{S}_{\text{hist-opt}}$) differ by a negligible amount. This observation is confirmed in Fig. 11, where we plot various histograms, reconstructed at 0.3 bps, for the *boiler* data set. The histograms produced by $\mathcal{S}_{\text{wav}}$ and $\mathcal{S}_{\text{hist-sig}}$ have approximately the same shape and are the closest to the reference histogram. The next best histogram is produced by $\mathcal{S}_{\text{lvl}}$, followed by the one produced by $\mathcal{S}_{\text{bit}}$, and finally $\mathcal{S}_{\text{mag}}$. These results suggest that histogram computation benefits from a bit ordering that combines both resolution and precision, with a strong bias toward precision.

4.4 Isosurface Extraction

Studying isosurfaces of a given function is an essential task in many visualization and analysis pipelines, as they can highlight features of interest. For measuring error between isosurfaces, we have found that the commonly used Hausdorff distance does not work well in our case, because two very different reconstructed surfaces may share the same Hausdorff distance to the reference. More sophisticated metrics exist, focusing on different characteristics such as geometric [20] and topological [19] properties, but they assume the surface has certain properties. Since isosurfaces partition the domain into "inside" and "outside" regions, we opt for a simpler error metric that assumes nothing about the shape of the isosurfaces, but simply counts misclassified voxels. This metric differs from comparing histograms with two bins in that we care about the spatial position and not just voxel counts.

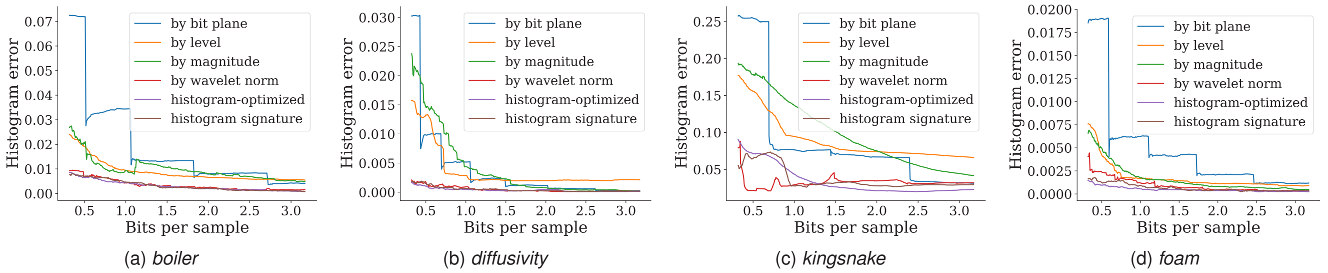

Fig. 10: Comparison of histogram errors among streams. Plots are truncated to highlight differences without hiding important trends. In general, in terms of error, $\mathcal{S}_{\text{hist-opt}} \approx \mathcal{S}_{\text{hist-sig}} \approx \mathcal{S}_{\text{wav}} < \mathcal{S}_{\text{lvl}}, \mathcal{S}_{\text{bit}}, \mathcal{S}_{\text{mag}}$. The erratic behavior at the beginning for *kingsnake* is likely due to the data being too noisy. The especially poor performances of $\mathcal{S}_{\text{bit}}$ for *boiler* and *foam* are due to the “shifting” effect explained in Section 4.2.1. Crossover points between $\mathcal{S}_{\text{bit}}$ and $\mathcal{S}_{\text{lvl}}$ are explained in Fig. 12.

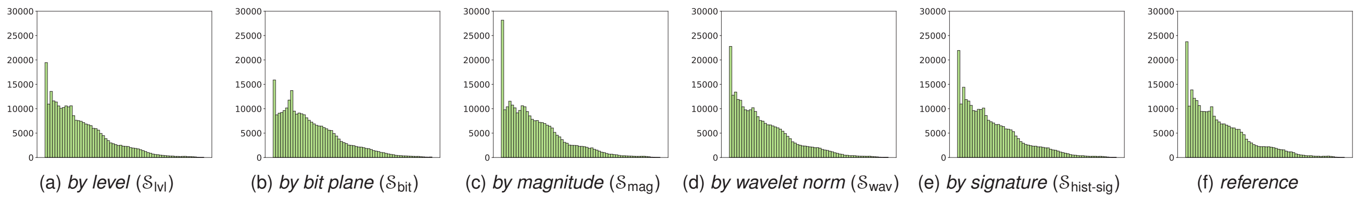

Fig. 11: Histograms of the *boiler* data set, reconstructed at 0.3 bps. $\mathcal{S}_{\text{lvl}}$, $\mathcal{S}_{\text{wav}}$, and $\mathcal{S}_{\text{hist-sig}}$ produce histograms that share a shape similar to the reference histogram, with most of the peaks and valleys preserved. In contrast, $\mathcal{S}_{\text{bit}}$ produces a spurious peak not found in the reference. Finally, $\mathcal{S}_{\text{mag}}$'s histogram has a widely skewed distribution where too many values fall into the first bin.

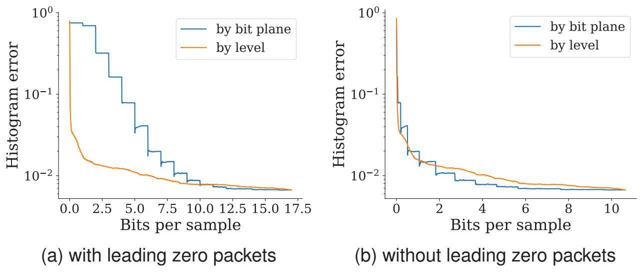

Fig. 12: Histogram error curves produced by $\mathcal{S}_{\text{bit}}$ and $\mathcal{S}_{\text{lvl}}$, for *boiler*, with and without leading zero bits. The vertical axis is in log scale. The error for $\mathcal{S}_{\text{bit}}$ reduces in a stair-step fashion, where each step corresponds to a new bit plane streamed. $\mathcal{S}_{\text{bit}}$ benefits significantly more from the removal of leading zero bits (the blue curve shifts more to the left).

However, if the error caused by discarding a packet is of subvoxel resolution, such a metric fails to capture the importance of that packet, causing $\mathcal{S}_{\text{iso-opt}}$ to be ineffective. Therefore, we add the relative difference in surface areas ($|A_1 - A_2|/|A_1|$) to the error term. This additional term is often between $[0,1]$ and is meant to capture the subvoxel error when the number of misclassified voxels is zero.

With the error metric defined, we can compute a data-dependent stream optimized for this metric ($\mathcal{S}_{\text{iso-opt}}$) and a stream based on its signature ($\mathcal{S}_{\text{iso-sig}}$) using Algorithm 1 and Algorithm 2. Fig. 13 compares the performances of these two streams, along with $\mathcal{S}_{\text{bit}}$, $\mathcal{S}_{\text{lvl}}$, $\mathcal{S}_{\text{wav}}$, and $\mathcal{S}_{\text{mag}}$. As can be observed, $\mathcal{S}_{\text{lvl}}$ performs poorly, indicating that isosurface extraction, requires higher levels of resolution compared to histogram computation, as we need to resolve a surface in the spatial domain and not just the range domain of the function. $\mathcal{S}_{\text{wav}}$ and $\mathcal{S}_{\text{iso-sig}}$ typically outperform $\mathcal{S}_{\text{bit}}$, especially at low bit rates. Fig. 14 renders the isosurfaces reconstructed at 0.6 bps for all streams. In terms of the quality of the reconstructed surfaces, $\mathcal{S}_{\text{iso-sig}} \approx \mathcal{S}_{\text{wav}} > \mathcal{S}_{\text{bit}} > \mathcal{S}_{\text{mag}} > \mathcal{S}_{\text{lvl}}$, which agrees with the plots in Fig. 13. For isosurface extraction, $\mathcal{S}_{\text{wav}}$ appears to be the only stream — among the data-independent ones — that consistently works well in all cases.

5 Discussion and Future Work

This work addresses one of the biggest contemporary challenges in visualization: management of the enormous amounts of data. We focus on the trade-off between two prominent dimensions of data reduction, resolution and precision, with respect to common analysis and visualization tasks. To keep the study tractable while not compromising the generalizability of results, we target fundamental analysis and visualization tasks, with an outlook that these can serve as building blocks for more complex and multiparameter tasks in the future. Although the paper focuses on a small set of core tasks, the framework is generic and applies to any well-defined metric, and one future direction is to consider a broader set of tasks.

We present the first empirical study to demonstrate that combining reduction in precision and resolution can lead to a significant improvement in data quality for the same data budget, and that different tasks might prefer different resolution-versus-precision trade-offs. For example, whereas computing histograms requires high precision, computing derivatives benefits more from higher resolution, and function reconstruction and isosurface extraction require a suitable mix of the two (see Fig. 15). We also show that common reduction techniques, e.g., those based on $\mathcal{S}_{\text{lvl}}$ and $\mathcal{S}_{\text{mag}}$, do not perform well when leading zero bits are removed (to simulate entropy compression). For each task, the relative ordering of the rate-distortion curves stays largely the same regardless of data sets, although the gaps among them vary depending on the smoothness and noisiness of the data. Compared to data-independent streams, signature-based streams often perform better because they can adapt to the data. They are also amenable for implementation (unlike $\mathcal{S}_{\text{opt}}$), since a signature is negligibly small and thus can be precomputed and stored during preprocessing. It is also interesting to consider per-block signatures instead of a global one.

An important question is whether task- and data-dependent streams provide sufficient advantages over purely data-independent streams. In practice, data would be used for multiple, and not necessarily predefined, tasks, and maintaining multiple streams will likely lead to additional overheads. Here, we consider $\mathcal{S}_{\text{sig}}$ to be the best possible stream that could be realized. Improvements on $\mathcal{S}_{\text{sig}}$ in the resolution-versus-precision space are likely possible, but they are unlikely to be significant. Given these assumptions and the fact that $\mathcal{S}_{\text{sig}}$ in most cases provides very similar results to $\mathcal{S}_{\text{bit}}$ or $\mathcal{S}_{\text{wav}}$, the additional effort (and potential overheads) for task-dependent bit orderings is unlikely to be beneficial. This leaves a significant gap between the best data-independent streams and the optimal stream $\mathcal{S}_{\text{opt}}$. Our experiments suggest that the majority of these differences can be attributed to spatial adaptivity (see Fig. 15). The prototypical example is isosurface computation, where $\mathcal{S}_{\text{opt}}$ can skip all regions that do not affect any portion of the surface. It may be worthwhile in future work to investigate solutions to spatial adaptivity to significantly improve the

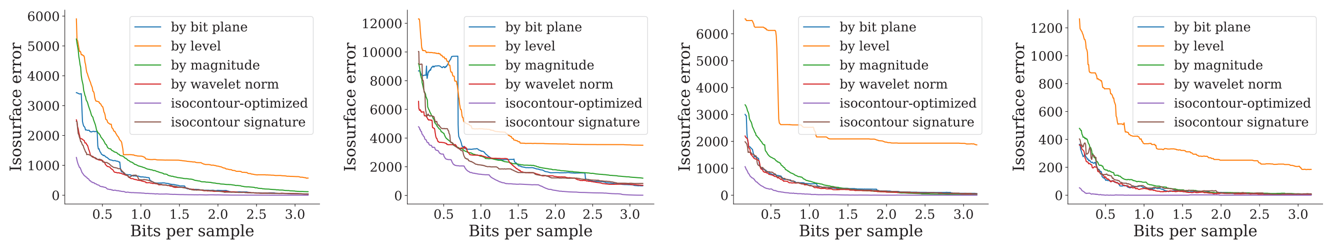

(a) *pressure, #cells = 36149* (b) *kingsnake, #cells = 45783* (c) *plasma, #cells = 24856* (d) *turbulence, #cells = 33742*

Fig. 13: Comparison of isosurface errors among streams. Plots are truncated to highlight differences without hiding important trends. The number of cells that each original surface occupies is reported. The trend in error is $\mathcal{S}_{\text{iso-opt}} < \mathcal{S}_{\text{iso-sig}} \approx \mathcal{S}_{\text{wav}} < \mathcal{S}_{\text{bit}} < \mathcal{S}_{\text{mag}} << \mathcal{S}_{\text{lvl}}$.

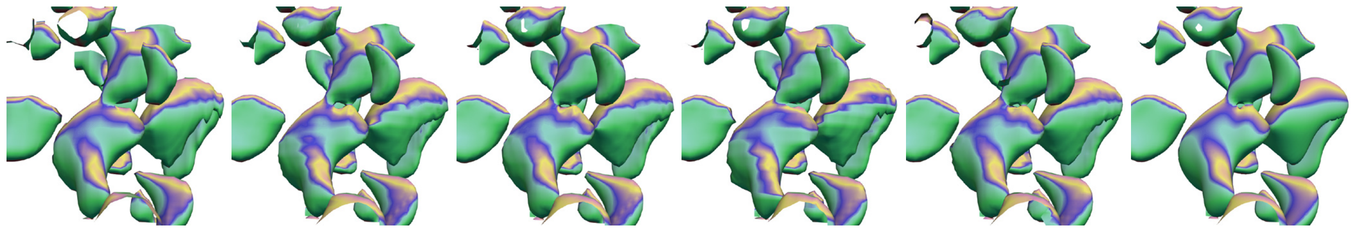

(a) *by level* ($\mathcal{S}_{\text{lvl}}$) (b) *by bit plane* ($\mathcal{S}_{\text{bit}}$) (c) *by wavelet norm* ($\mathcal{S}_{\text{wav}}$) (d) *by magnitude* ($\mathcal{S}_{\text{mag}}$) (e) *by signature* ($\mathcal{S}_{\text{iso-sig}}$) (f) *reference*

Fig. 14: Rendering of isosurfaces at isovalue of 0.2, at 0.6 bps, for the *pressure* data set. The surfaces are colored by the x-component of the normal vector at each point. $\mathcal{S}_{\text{wav}}$ and $\mathcal{S}_{\text{iso-sig}}$ produce surfaces that are closest to the reference, followed by $\mathcal{S}_{\text{bit}}$, $\mathcal{S}_{\text{mag}}$, and $\mathcal{S}_{\text{lvl}}$.

performance of data-independent streams.

This study can be considered only a first step toward a system of solutions that can optimize storage, network, and I/O bandwidth to suit specific tasks at hand. Ultimately, our results can guide development of new data layouts and file formats for scientific data. $\mathcal{S}_{\text{wav}}$ appears to provide the best all around performance. However, for a file format additional constraints must be considered, such as disk block sizes, cache coherence, and compression. Furthermore, an ideal format should allow task-dependent data queries even though task-dependent formats will likely be restricted to very specific situations.

Finally, for fair comparisons, we always reconstruct the data at full resolution using wavelets. However, processing and memory costs are important, and it is likely that adaptive representations would be used in practice [16, 25, 46]. In these cases the error of a given approximation depends not only on the available information, but also on the data structure and algorithm being used. For example, trilinear interpolation on a coarse grid might produce different results than wavelet reconstruction on the original mesh. There exist solutions where both interpolations are equivalent [67], but such solutions have not yet been implemented in standard tools. An important future research direction will be to understand the implications of the results presented here for existing toolchains such as VTK.

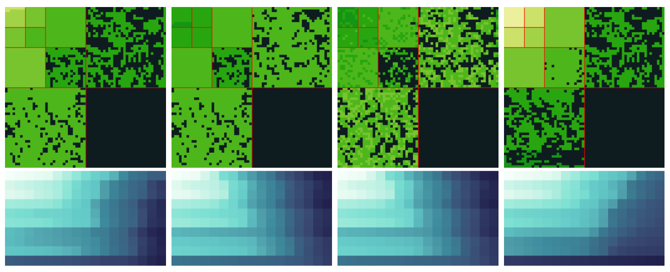

(a) $\mathcal{S}_{\text{rmse-sig}}$ (b) $\mathcal{S}_{\text{lap-sig}}$ (c) $\mathcal{S}_{\text{lap-opt}}$ (d) $\mathcal{S}_{\text{hist-sig}}$

Fig. 15: (Top) Bit distribution across subbands at 1.6 bps for signature-based streams, and (bottom) corresponding stream signatures. The data is a 2D slice from *diffusivity*. Subbands are separated by red lines. The color of each pixel indicates the bit plane at which the corresponding coefficient currently is. Brighter greens correspond to more precision. Both the top and the bottom rows show that $\mathcal{S}_{\text{hist-sig}}$ allocates more bits to the lower subbands, while $\mathcal{S}_{\text{lap-sig}}$ prefers to stream bits from higher subbands. $\mathcal{S}_{\text{rmse-sig}}$ is somewhere in the middle. Both $\mathcal{S}_{\text{lap-sig}}$ and $\mathcal{S}_{\text{lap-opt}}$ share the same signature by definition but only $\mathcal{S}_{\text{lap-opt}}$ provides spatial adaptivity, seen as nonuniform colors in each subband.

A L2 Norms of CDF5/3 wavelet basis functions

The $\mathcal{S}_{\text{wav}}$ stream requires the norms of CDF5/3 wavelet basis functions, which the following pseudocode computes (in 1D).

```
sca_weights = [1/2, 1, 1/2]
wav_weights = [-1/8, -1/4, 3/4, -1/4, -1/8]
scal_func = sca_weights, wav_func = wav_weights
sca_norms = [], wav_norms = []
for (l = 0; l < n+1; l = l+1) {
  sca_norms[l] = norm(sca_func), wav_norms[l] = norm(wav_func)
  wav_weights = upsample(wav_weights)
  wav_func = convolve(wav_weights, sca_func)
  sca_weights = upsample(sca_weights)
  sca_func = convolve(sca_weights, sca_func) }
```

The `upsample` function adds a 0 between every two adjacent samples in its argument. The `convolve` function implements the convolution operation in 1D. When the loop ends, `sca_norms[n]` stores the the norm of the basis functions in the coarsest subband (they all share the same norm), while `wav_norms[n-1]`, `wav_norms[n-2]`, . . . store the norms of basis functions in subsequent subbands, from coarse to fine. Since we use tensor product wavelets, the norms of basis functions in higher dimensions are simply products of the 1D norms.

Acknowledgments

We thank the reviewers for their valueable comments. Some of the data sets are kindly shared with us by Benjamin Isaac (*boiler*) and Kristoffer Matheson and Ashley Spear (*foam* – collected through work supported by NSF grant DMREF-1629660). This work was performed under the auspices of the U.S. Department of Energy by Lawrence Livermore National Laboratory under Contract DE-AC52-07NA27344 and was supported by the LLNL-LDRD Program under Project No. 17-SI-004. This work is supported in part by NSF: CGV: Award:1314896, NSF:IIP Award :1602127 NSF:ACI:award 1649923, DOE/SciDAC DESC0007446, CCMSC DE-NA0002375, and PIPER: ER26142 DE-SC0010498. This material is based upon work supported by the Department of Energy, National Nuclear Security Administration, under Award Number(s) DE-NA0002375. This work was also supported by the Department of Energy Office of Science, Office of Advanced Scientific Computing Research under the guidance of Dr. Lucy Nowell.

References

[1] A. H. Baker, H. Xu, J. M. Dennis, M. N. Levy, D. Nychka, S. A. Mickelson, J. Edwards, M. Vertenstein, and A. Wegener. A methodology for evaluating

the impact of data compression on climate simulation data. In *International Symposium on High-performance Parallel and Distributed Computing*, pp. 203–214, 2014.

[2] R. Ballester-Ripoll and R. Pajarola. Lossy volume compression using Tucker truncation and thresholding. *The Visual Computer*, 32(11):1433–1446, 2016.

[3] R. Ballester-Ripoll, S. K. Suter, and R. Pajarola. Analysis of tensor approximation for compression-domain volume visualization. *Computers & Graphics*, 47(C):34–47, 2015.

[4] M. Balsa Rodríguez, E. Gobbetti, J. Iglesias Guitián, M. Makhinya, F. Marton, R. Pajarola, and S. Suter. State-of-the-art in compressed GPU-based direct volume rendering. *Computer Graphics Forum*, 33(6):77–100, 2014.

[5] M. J. Berger and P. Colella. Local adaptive mesh refinement for shock hydrodynamics. *Journal of Computational Physics*, 82(1):64–84, 1989.

[6] J. Beyer, M. Hadwiger, and H. Pfister. State-of-the-art in GPU-based large-scale volume visualization. *Computer Graphics Forum*, 34(8):13–37, 2015.

[7] A. Bhattacharyya. On a measure of divergence between two statistical populations defined by their probability distributions. *Bulletin of the Calcutta Mathematical Society*, 35:99–109, 1943.

[8] P. Burt and E. Adelson. The Laplacian pyramid as a compact image code. *IEEE Transactions on Communications*, 31(4):532–540, 1983.

[9] J. Calhoun, F. Cappello, L. N. Olson, M. Snir, and W. D. Gropp. Exploring the feasibility of lossy compression for PDE simulations. *The International Journal of High Performance Computing Applications*, 27, 2018.

[10] Y. Cho and W. A. Pearlman. Quantifying the coding performance of zerotrees of wavelet coefficients: Degree-k zerotree. *IEEE Transactions on Signal Processing*, 55(6):2425–2431, 2007.

[11] C. Chrysafis, A. Said, A. Drukarev, A. Islam, and W. A. Pearlman. SBHP-a low complexity wavelet coder. In *IEEE International Conference on Acoustics, Speech, and Signal Processing*, vol. 6, pp. 2035–2038, 2000.

[12] J. Clyne. The multiresolution toolkit: Progressive access for regular gridded data. In *Visualization, Imaging, and Image Processing*, pp. 152–157, 2003.

[13] J. Clyne, P. Mininni, A. Norton, and M. Rast. Interactive desktop analysis of high resolution simulations: Application to turbulent plume dynamics and current sheet formation. *New Journal of Physics*, 9(8):301, 2007.

[14] A. Cohen, I. Daubechies, and J. Feauveau. Biorthogonal bases of compactly supported wavelets. *Communications on Pure and Applied Mathematics*, 45(5):485–560, 1992.

[15] A. W. Cook, W. Cabot, and P. L. Miller. The mixing transition in Rayleigh-Taylor instability. *Journal of Fluid Mechanics*, 511:333–362, 2004.

[16] C. Crassin, F. Neyret, S. Lefebvre, and E. Eisemann. Gigavoxels: Ray-guided streaming for efficient and detailed voxel rendering. In *ACM SIGGRAPH Symposium on Interactive 3D Graphics and Games*, pp. 15–22, 2009.

[17] D. A. Donzis, P. Yeung, and D. Pekurovsky. Turbulence simulations on $\mathcal{O}(10^4)$ processors. In *TeraGrid*, 2008.

[18] T. Etiene, D. Jönsson, T. Ropinski, C. Scheidegger, J. L. D. Comba, L. G. Nonato, R. M. Kirby, A. Ynnerman, and C. T. Silva. Verifying volume rendering using discretization error analysis. *IEEE Transactions on Visualization and Computer Graphics*, 20(1):140–154, 2014.

[19] T. Etiene, L. G. Nonato, C. Scheidegger, J. Tienry, T. J. Peters, V. Pascucci, R. M. Kirby, and C. T. Silva. Topology verification for isosurface extraction. *IEEE Transactions on Visualization and Computer Graphics*, 18(6):952–965, 2012.

[20] T. Etiene, C. Scheidegger, L. G. Nonato, R. M. Kirby, and C. Silva. Verifiable visualization for isosurface extraction. *IEEE Transactions on Visualization and Computer Graphics*, 15(6):1227–1234, 2009.

[21] T. Fogal, H. Childs, S. Shankar, J. Krüger, R. D. Bergeron, and P. Hatcher. Large data visualization on distributed memory multi-GPU clusters. In *High Performance Graphics*, pp. 57–66, 2010.

[22] T. Fogal, A. Schiewe, and J. Krüger. An Analysis of Scalable GPU-Based Ray-Guided Volume Rendering. In *IEEE Symposium on Large-Scale Data Analysis and Visualization*, 2013.

[23] N. Fout and K. L. Ma. Transform coding for hardware-accelerated volume rendering. *IEEE Transactions on Visualization and Computer Graphics*, 13(6):1600–1607, 2007.

[24] E. Gobbetti, J. A. Iglesias Guitián, and F. Marton. COVRA: A compression-domain output-sensitive volume rendering architecture based on a sparse representation of voxel blocks. *Computer Graphics Forum*, 31(34):1315–1324, 2012.

[25] E. Gobbetti, F. Marton, and J. A. Iglesias Guitián. A single-pass GPU ray casting framework for interactive out-of-core rendering of massive volumetric datasets. *The Visual Computer*, 24(7):797–806, 2008.

[26] Z. Gong, T. Rogers, J. Jenkins, H. Kolla, S. Ethier, J. Chen, R. Ross, S. Klasky, and N. F. Samatova. MLOC: Multi-level layout optimization framework for compressed scientific data exploration with heterogeneous access patterns. In *International Conference on Parallel Processing*, pp. 239–248, 2012.

[27] A. Gosselin-Ildari. The deep scaly project, "lampropeltis getula" (on-line), digital morphology. `http://digimorph.org/specimens/Lampropeltis_getula/adult/` (accessed on July 23, 2018), 2006.

[28] F. Guo, H. Li, W. Daughton, and Y.-H. Liu. Formation of hard power-laws in the energetic particle spectra resulting from relativistic magnetic reconnection. *Physical Review Letters*, 113, 2014.

[29] S. Guthe and W. Strasser. Advanced techniques for high-quality multi-resolution volume rendering. *Computers & Graphics*, 28(1):51 – 58, 2004.

[30] S. Guthe, M. Wand, J. Gonser, and W. Strasser. Interactive rendering of large volume data sets. In *IEEE Visualization*, pp. 53–60, 2002.

[31] M. Hadwiger, J. Beyer, W. K. Jeong, and H. Pfister. Interactive volume exploration of petascale microscopy data streams using a visualization-driven virtual memory approach. *IEEE Transactions on Visualization and Computer Graphics*, 18(12):2285–2294, 2012.

[32] E. Hellinger. Neue begründung der theorie quadratischer formen von unendlichvielen veränderlichen. *Journal für die reine und angewandte Mathematik*, 136:210–271, 1909.

[33] I. Ihm and S. Park. Wavelet-based 3D compression scheme for interactive visualization of very large volume data. *Computer Graphics Forum*, 18(1):3–15, 2003.

[34] J. Iverson, C. Kamath, and G. Karypis. Fast and effective lossy compression algorithms for scientific datasets. In *International Conference on Parallel Processing*, pp. 843–856, 2012.

[35] S. Kullback and R. A. Leibler. On information and sufficiency. *The Annals of Mathematical Statistics*, 22(1):79–86, 1951.

[36] S. Lakshminarasimhan, N. Shah, S. Ethier, S. Klasky, R. Latham, R. Ross, and N. F. Samatova. Compressing the incompressible with ISABELA: In-situ reduction of spatio-temporal data. In *International European Conference on Parallel and Distributed Computing*, pp. 366–379, 2011.

[37] E. LaMar, B. Hamann, and K. I. Joy. Multiresolution techniques for interactive texture-based volume visualization. In *IEEE Visualization*, pp. 355–361, 1999.

[38] D. E. Laney, S. Langer, C. Weber, P. Lindstrom, and A. Wegener. Assessing the effects of data compression in simulations using physically motivated metrics. In *International Conference for High Performance Computing, Networking, Storage and Analysis*, pp. 1–12, 2013.

[39] S. Li, K. Gruchalla, K. Potter, J. Clyne, and H. Childs. Evaluating the efficacy of wavelet configurations on turbulent-flow data. In *IEEE Symposium on Large Data Analysis and Visualization*, pp. 81–89, 2015.

[40] S. Li, N. Marsaglia, C. Garth, J. Woodring, J. Clyne, and H. Childs. Data reduction techniques for simulation, visualization and data analysis. *Computer Graphics Forum*, 37(6):422–447, 2018.

[41] P. Lindstrom. Fixed-rate compressed floating-point arrays. *IEEE Transactions on Visualization and Computer Graphics*, 20(12):2674–2683, 2014.

[42] P. Lindstrom. Reducing data movement using adaptive-rate computing, 2018. `https://computation.llnl.gov/sites/default/files/public//llnl-post-728998.pdf` (accessed on June 13, 2018).

[43] P. Lindstrom and M. Isenburg. Fast and efficient compression of floating-point data. *IEEE Transactions on Visualization and Computer Graphics*, 12(5):1245–1250, 2006.

[44] P. Ljung, C. Lundstrom, A. Ynnerman, and K. Museth. Transfer function based adaptive decompression for volume rendering of large medical data sets. In *IEEE Symposium on Volume Visualization and Graphics*, pp. 25–32, 2004.

[45] K. E. Matheson, K. K. Cross, M. M. Nowell, and A. D. Spear. A multiscale comparison of stochastic open-cell aluminum foam produced via conventional and additive-manufacturing routes. *Materials Science and Engineering: A*, 707:181–192, 2017.

[46] K. Museth. VDB: High-resolution sparse volumes with dynamic topology. *ACM Transaction on Graphics*, 32(3):1–22, 2013.

[47] K. G. Nguyen and D. Saupe. Rapid high quality compression of volume data for visualization. *Computer Graphics Forum*, 20(3):49–57, 2002.

[48] P. Ning and L. Hesselink. Vector quantization for volume rendering. In *Workshop on Volume Visualization*, pp. 69–74, 1992.

[49] V. Pascucci and R. J. Frank. Global static indexing for real-time exploration of very large regular grids. In *ACM/IEEE Supercomputing*, pp. 45–45, 2001.

[50] W. A. Pearlman, A. Islam, N. Nagaraj, and A. Said. Efficient, low-complexity image coding with a set-partitioning embedded block coder. *IEEE Transactions on Circuits and Systems for Video Technology*, 14(11):1219–1235, 2004.

[51] S. Prohaska, A. Hutanu, R. Kahler, and H. C. Hege. Interactive exploration of large remote micro-CT scans. In *IEEE Visualization*, pp. 345–352, 2004.

[52] F. Reichl, M. Treib, and R. Westermann. Visualization of big SPH simulations via compressed octree grids. In *IEEE International Conference on Big Data*, pp. 71–78, 2013.

[53] Y. Rubner, C. Tomasi, and L. J. Guibas. A metric for distributions with applications to image databases. In *International Conference on Computer Vision*, pp. 59–66, 1998.

[54] A. Said and W. A. Pearlman. A new, fast, and efficient image codec based on set partitioning in hierarchical trees. *IEEE Transactions on Circuits and Systems for Video Technology*, 6(3):243–250, 1996.

[55] H. Samet. The quadtree and related hierarchical data structures. *ACM Computing Surveys*, 16(2):187–260, 1984.

[56] J. Schneider and R. Westermann. Compression domain volume rendering. In *IEEE Visualization*, pp. 293–300, 2003.

[57] N. Smirnov. Table for estimating the goodness of fit of empirical distributions. *Annals of Mathematical Statistics*, 19(2):279–281, 1948.

[58] P. Smith, J. Thornock, Y. Wu, S. Smith, and B. Isaac. Oxy-coal power boiler simulation and validation through extreme computing. In *International Conference on Numerical Combustion*, 2015.

[59] S. K. Suter, J. A. I. Guitian, F. Marton, M. Agus, A. Elsener, C. P. E. Zollikofer, M. Gopi, E. Gobbetti, and R. Pajarola. Interactive multiscale tensor reconstruction for multiresolution volume visualization. *IEEE Transactions on Visualization and Computer Graphics*, 17(12):2135–2143, 2011.

[60] S. K. Suter, M. Makhynia, and R. Pajarola. Tamresh - tensor approximation multiresolution hierarchy for interactive volume visualization. In *EG/VGTC Conference on Visualization*, pp. 151–160, 2013.

[61] M. J. Swain and D. H. Ballard. Color indexing. *International Journal of Computer Vision*, 7(1):11–32, 1991.

[62] D. Tao, S. Di, Z. Chen, and F. Cappello. Significantly improving lossy compression for scientific data sets based on multidimensional prediction and error-controlled quantization. In *IEEE International Parallel and Distributed Processing Symposium*, pp. 1129–1139, 2017.

[63] D. Tao, S. Di, H. Guo, Z. Chen, and F. Cappello. Z-checker: A framework for assessing lossy compression of scientific data. *The International Journal of High Performance Computing Applications*, 2017.

[64] D. S. Taubman and M. W. Marcellin. *JPEG 2000: Image Compression Fundamentals, Standards and Practice*. Springer, 2001.

[65] M. Treib, K. Bürger, F. Reichl, C. Meneveau, A. Szalay, and R. Westermann. Turbulence visualization at the terascale on desktop PCs. *IEEE Transactions on Visualization and Computer Graphics*, 18(12):2169–2177, 2012.

[66] C. Wang and K. L. Ma. A statistical approach to volume data quality assessment. *IEEE Transactions on Visualization and Computer Graphics*, 14(3):590–602, 2008.

[67] K. Weiss and P. Lindstrom. Adaptive multilinear tensor product wavelets. *IEEE Transactions on Visualization and Computer Graphics*, 22(1):985–994, 2016.

[68] R. Westermann. A multiresolution framework for volume rendering. In *Symposium on Volume Visualization*, pp. 51–58, 1994.

[69] J. Woodring, J. Ahrens, J. Figg, J. Wendelberger, S. Habib, and K. Heitmann. In-situ sampling of a large-scale particle simulation for interactive visualization and analysis. In *EG/VGTC Conference on Visualization*, pp. 1151–1160, 2011.

[70] J. Woodring, S. Mniszewski, C. Brislawn, D. DeMarle, and J. Ahrens. Revisiting wavelet compression for large-scale climate data using JPEG 2000 and ensuring data precision. In *IEEE Symposium on Large Data Analysis and Visualization*, pp. 31–38, 2011.